Kinematic Modeling and Characterization of Soft Parallel Robots

Xinjia Huang, Xiangyang Zhu, *Member, IEEE*, and Guoying Gu, *Senior Member, IEEE*

***Abstract*—Parallel robots with rigid transmission mechanisms have been widely developed to improve the speed, precision, and load capability. However, it is still challenging in promoting soft parallel robots due to the difficulty in accurate kinematic modeling of soft continuum links. In this article, we present a general framework on the design, kinematic modeling, model-based characterization, and control for a class of soft parallel robots. The designed soft parallel robot consists of three fiber-reinforced soft pneumatic actuators, a base stage, and an output stage. With the introduction of the mathematical toolkit of the absolute nodal coordinate formulation, we develop a continuum-based model to describe and parameterize both the global complex configuration and the local large deformation of the soft parallel robot. In this sense, the mappings among the defined kinematic spaces of the robot can be characterized through force analysis. Based on the developed model, we next analyze the robot's workspace and stiffness with different design parameters, which are also verified by a set of experiments. Finally, we establish a model-based trajectory tracking controller for the soft parallel robot. The experimental results demonstrate that with the feedforward controller, the end effector of the soft parallel robot can well follow the desired trajectories under different output velocities, where the average positioning error is about 2.6–3.9% of the maximum length of the workspace.**

***Index Terms*—Absolute nodal coordinate formulation, kinematic modeling, parallel mechanisms, soft robots.**

I. Introduction

SOFT robots are usually made from compliant materials with various actuation technology, such as compressed fluids [1], [2], cables [3], [4], shape memory alloys [5], [6], and electric fields [7], [8]. The features of manipulation safety, design diversity, and motion dexterity make soft robots promising in the applications of environment exploration, health-care, and human–robot interaction [9]–[11]. However, the benefits of compliance usually come with the reduction of load capability and stability of soft robots.

To achieve dexterous manipulations in planar or spatial spaces, soft manipulators are usually designed by cascading multiple robotic sections [12]–[14]. However, the slender serial soft mechanisms usually further reduce the robot's stiffness and output forces. In order to maintain the natural compliance of materials, and meanwhile, obtain acceptable stiffness in applications, some variable stiffness structures and mechanisms have been recently reported, such as by applying shape memory alloy [6] and particle jamming [15]. Unfortunately, these methods generally make the hardware of soft robotic systems complex and increase the difficulty and cost in fabrication.

In the field of rigid robots, parallel mechanisms are usually utilized to achieve the high stiffness, output force, speed, and precision [16], [17]. Inspired by these achievements, similar design methods have also been spread into the field of soft robotics. To the best of our knowledge, the term of soft parallel robot is first introduced in 2009 [18] as the parallel robots with links made from cables or tendons. Recently, various other designs of soft parallel robots have been reported by applying soft links [19], [20], soft joints [21], [22], and both soft links and joints [23], [24]. Due to their compliance in material and acceptable stiffness in parallel designs, soft parallel robots show the promise applications of human–robot interaction, such as extracorporeal ultrasound [25] and rehabilitation [26]. However, when coupled with soft kinematic chains, the robots theoretically have infinite degrees of freedom, which makes the kinematic modeling challenging, especially at the large deformation conditions.

To address this challenge, many kinematic models have been reported for soft robots, which can be roughly divided into two categories, i.e., robot-independent models and robot-dependent models. Robot-independent models mainly focus on the representation of robotic motions purely in geometry without considering the used materials and actuation. The adopted techniques in these models usually include piecewise constant curvature approaches [12], [27], mode shape function approaches [28], [29], Euler spiral approaches [30], and Pythagorean hodograph curve approaches [31] to approximate the shape of the robot backbones. For serial multisectional soft robots, each section of which can be actuated and controlled separately, these models are convenient to be applied for the kinematics description and feedback control tasks. However, for soft robots with more complex designs, such as soft parallel robots, the deformations of each part of soft kinematic chains are coupled by the elasticity

Manuscript received November 26, 2021; revised April 26, 2022; accepted May 5, 2022. This work was supported in part by the National Natural Science Foundation of China under Grant 52025057 and Grant 91848204, and in part by the Science and Technology Commission of Shanghai Municipality under Grant 20550712100. This paper was recommended for publication by Associate Editor Yajing Shen and Editor Arianna Menciassi upon evaluation of the reviewers' comments. *(Corresponding author: Guoying Gu.)*

The authors are with the State Key Laboratory of Mechanical System and Vibration, School of Mechanical Engineering, Shanghai Jiao Tong University, Shanghai 200240, China, and also with the Meta Robotics Institute, Shanghai Jiao Tong University, Shanghai 200240, China (e-mail: huangxinjia@sjtu.edu.cn; mexyzhu@sjtu.edu.cn; guguoying@sjtu.edu.cn).

This article has supplementary material provided by the authors and color versions of one or more figures available at https://doi.org/10.1109/TRO.2022.3174474.

Digital Object Identifier 10.1109/TRO.2022.3174474

and constraint forces. Such coupling principle directly depends on the robot structure and properties of materials, moreover, the motions of individual robot component cannot be analyzed and controlled separately. On the other hand, the robot-dependent models can handle this issue. Among them, continuous Cosserat models [32]–[35] and continuous Euler–Bernoulli beam models [36], [37] are representative examples in the infinite state space, which can exactly describe the continuous deformation by partial differential equations. For the convenience of numeric implementation, some simplified approaches through finite state variables have also been developed, such as discretizing the continuous Cosserat models with geometrical approximation processes [38]–[40], or modeling the soft robot into lumped systems [41], [42]. These simplified models are mainly utilized for the forward simulation of the slender serial multisectional soft robots, but the model-based continuum shape control and the fast configuration prediction of soft robots with more general designs are still difficult.

Except for all the aforementioned models, absolute nodal coordinate formulation (ANCF) is a discrete modeling approach, which can describe the complex shapes of the deformed bodies with the use of the position and position gradients as coordinates [43]–[46]. Due to its accuracy of 3-D deformation descriptions and computational efficiency in handling external forces, it is usually used to parameterize various continuum models (such as flexible beams or plates [43]). The achievement of ANCF in the dynamic analysis of rubber-like structures [47] further demonstrates its potential in the modeling of soft robots. In our previous work, we have used the ANCF for kinematic modeling of planar soft robots for both fast motion simulation and feedforward control with external forces [48]. It should be noted that, in this reported model, the complete description of deformation for the 3-D structure is not considered. In this article, we aim to utilize the spatial position gradients to extend this approach for a general kinematics modeling framework of 3-D soft deformable mechanisms, and apply it for the simulation, characterization, and control of soft parallel robots. To this end, we first design a soft parallel robot composed of three soft fiber-reinforced pneumatic actuators, a base stage, and an output stage. Then, the kinematic mappings between the actuation space (input pressures) and robot configuration are established based on ANCF, which can be simultaneously applied for motion simulation, inverse-kinematic analysis, and control. Using our model, the robot workspace and displacements with external payloads are analyzed, which is well verified by experimental results. Finally, the feedforward trajectory tracking control tests are performed to demonstrate the effectiveness of the model-based controllers.

The main contributions of this work can be summarized as follows.

1) We propose a new kinematics modeling framework for the 3-D soft deformable mechanisms based on ANCF. The developed model considers the elasticity, geometrical constraints, and external forces. It can simultaneously predict the robot's motion and be used for inverse-kinematic calculation.
2) We apply the developed model for the workspace and stiffness characterization of the soft parallel robots with different design parameters, and a model-based feedforward controller is established for trajectory tracking tasks. Both experimental and simulation results are presented for the verification.

The reminder of this article is organized as follows. In Section II, the design and fabrication of a kind of soft parallel robot is presented. Section III discusses the kinematic modeling of the soft parallel robot based on ANCF. Section IV discusses the workspace and stiffness analysis, as well as the feedforward control based on the developed model. Section V concludes this article.

II. Design and Fabrication

In this section, the design and fabrication of the soft parallel robot is introduced. As shown in Fig. 1(a), the robot uses three soft fiber-reinforced actuators to connect the base stage and the output stage. Each actuator is made of silicone rubber with a chamber. The fiber wound around the chamber is used to prevent the expansion of the actuator's cross section [49]. Each actuator is initially straight, and bends after assembling into the robot because of the constraint forces. With the elongation of actuators by the inflation of chambers, the robot can achieve various spatial motions [as shown in Fig. 1(b)].

Fig. 2 shows the following fabrication processes of the actuator:

1) fabricating a silicone rubber (ELASTOSIL M4601) tube by molding;
2) arranging the fiber around the tube;
3) fixing the fiber reinforcement by a layer of silicone rubber with another step of molding;
4) sealing the actuator with two end plates, one of which reserves an airport.

The total length of one actuator is 175 mm, the outer diameter is 18 mm, and the diameter of the chamber is 12 mm.

After fabrication, the two ends of each actuator are directly fixed on the base stage and the output stage. In addition, the distance D between each two actuators on the base stage is adjustable. In this work, we use a dimensionless parameter $\phi = D/L_f$ to characterize the design (as illustrated in Fig. 3), where L_f is a constant (153 mm) representing the flexible length of the soft actuator. Without losing generality, we set ϕ as 1 in the following sections, except for that in Section IV-E, where the influence of this parameter on the robot's performance is analyzed.

III. Kinematic Modeling

In this section, a kinematic model of the soft parallel robot is developed for the motion simulation and inverse kinematic calculation tasks. To this end, the robot motion and deformation are first described and parameterized. Then, the effects of the actuation force, elasticity, and external forces are analyzed. Finally, the kinematic mappings between input pressures and the robot configuration are derived.

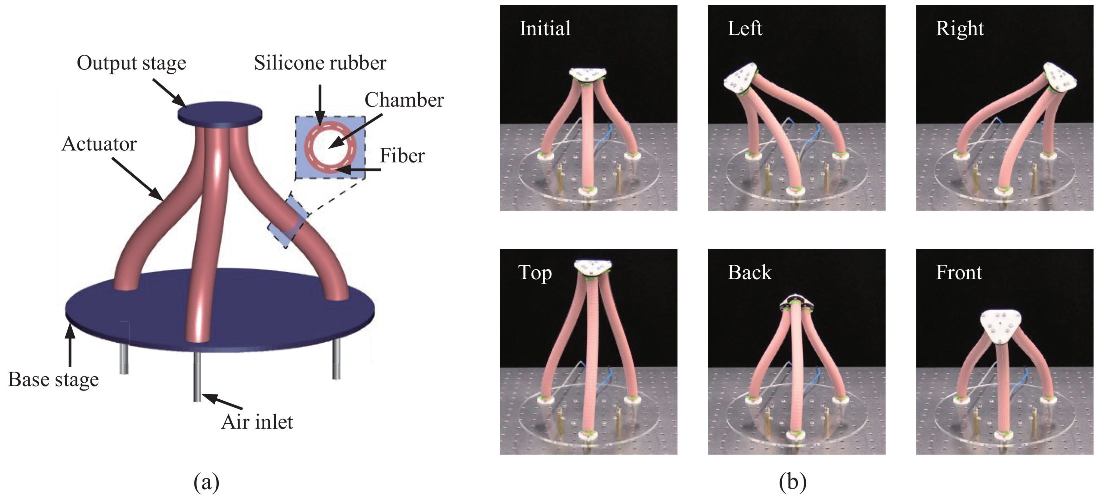

Fig. 1. Soft parallel robot. (a) The designed robot consists of three fiber-reinforced soft actuators, a base stage, and an output stage. (b) Pictures of the robot achieving different motions within its workspace.

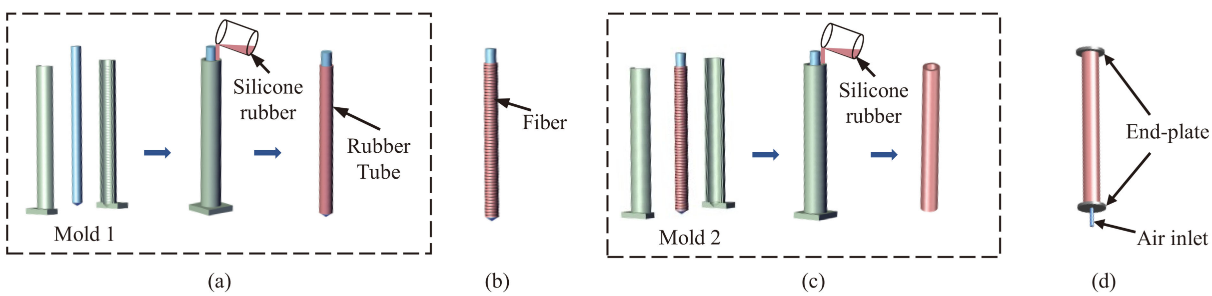

Fig. 2. Fabrication of the soft actuator. (a) Rubber tube is fabricated by molding. (b) Fiber is wound uniformly around the tube. (c) Second molding step is taken to encapsulate the actuator with a layer of silicone rubber and anchor all the fiber. (d) Actuator is sealed by two end plates, one of which reserves a port for the flow of air.

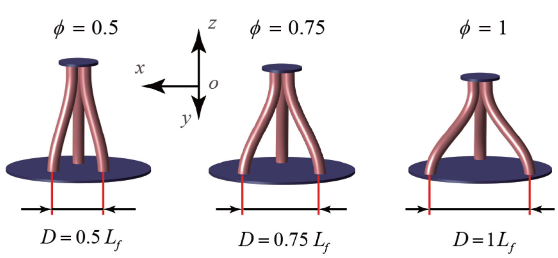

Fig. 3. Schematic illustration of the soft parallel robots with different values of the parameter ϕ.

A. Description of the Actuator Deformation

Soft actuators are usually designed to achieve certain desired motion mode. Typically, by arranging fiber angles, the soft fiber-reinforced actuators can generate various modes of motions, such as elongation, bending, or torsion [50], [51]. These motion modes are determined by the actuator's design without considering the external factors, which are called as inherent motion modes. In our design, as shown in Fig. 4, the inherent motion mode of the actuator behaves as elongation. After being assembled into the soft parallel robot, additional passive deformation will yield on the actuators due to the size difference between the base stage and the output stage. The passive deformation depends on the geometrical constraints (such as the design parameter ϕ), which can be used to adjust the robot performance (including the stiffness and the workspace). However, existing works about the modeling and analysis of soft actuators mainly focus on the inherent motion modes, and rare works investigate the bending or torsion behavior for an elongating actuator. In the following development, we will propose a new modeling approach for the soft parallel robot by taking both the inherent motions and the passive ones into consideration.

B. Parameterization of the Motion and Deformation

In order to establish the kinematics of the soft parallel robot, both the global configuration and local deformation of the robot should be firsty parameterized. To handle this issue in an efficient way, we use the position and the position gradient of ANCF [43]–[45].

For the use of ANCF, we discretize each soft actuator into several elements along its axial centerline. As shown in Fig. 5, for each element, a local spatial coordinate system ($O-XYZ$)

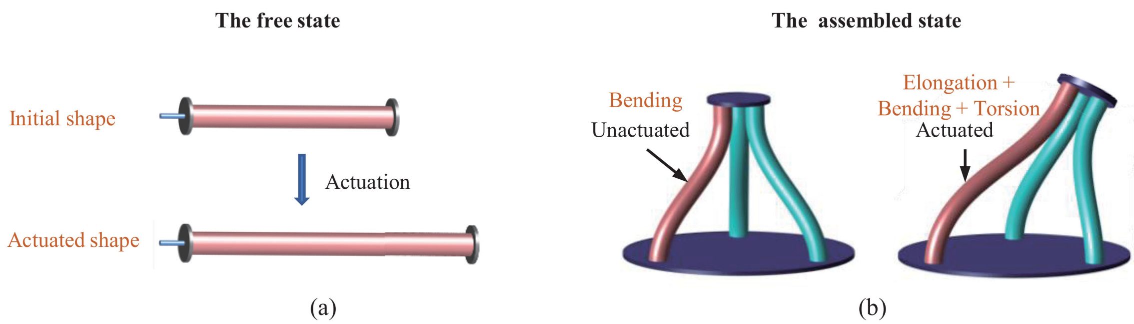

Fig. 4. Schematic illustration of the actuator's deformation in the free state and the assembled state.

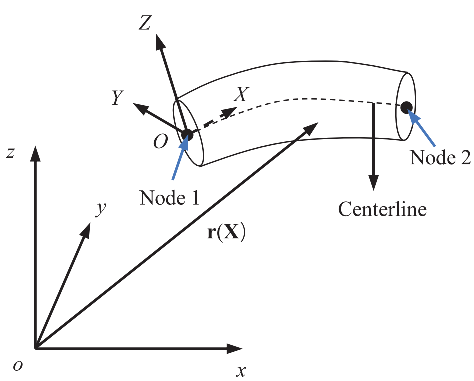

Fig. 5. Schematic illustration of the defined local coordinate system and global coordinate system for configuration parameterization.

is established, where $X \in [0, L_e]$ is the coordinate along the actuator's axis, and Y and Z are two coordinates perpendicular to X. The vector $\mathbf{X} \in \mathbb{R}^3$ defined in this coordinate system can be used to represent an arbitrary point in the element. Then, the motion of the element can be completely described by a vector-valued function $\mathbf{r}(\mathbf{X}) \in \mathbb{R}^3$ defined in the global coordinate system ($o - xyz$). In order to express $\mathbf{r}(\mathbf{X})$ conveniently, the position and position gradients of the element's nodes should be determined. For the ith node ($i = 1, 2$) of an element, the absolute coordinates can be defined as

$$\mathbf{q}_i \in \mathbb{R}^{12} = \left[{\mathbf{r}_i}^T \; {\mathbf{r}_{iX}}^T \; {\mathbf{r}_{iY}}^T \; {\mathbf{r}_{iZ}}^T \right]^T \tag{1}$$

where $\mathbf{r}_i$ is the nodal position vector, and $\mathbf{r}_{il} = \partial \mathbf{r} / \partial l$ ($l = X, Y, Z$) is the position gradient vector defined at the node. Then, the absolute nodal coordinates of the element can be expressed as

$$\mathbf{q}^e \in \mathbb{R}^{24} = \left[{\mathbf{q}_1}^T \; {\mathbf{q}_2}^T \right]^T. \tag{2}$$

Then, according to the polynomial interpolation method originally proposed by Shabana, *et al.* in [45], we can assume the displacement field $\mathbf{r}(\mathbf{X})$ as following polynomials

$$\mathbf{r}(\mathbf{X}) = \begin{bmatrix} a_1 + a_2 X + a_3 X^2 + a_4 X^3 + a_5 Y + \\ a_6 Z + a_7 XY + a_8 XZ \\ b_1 + b_2 X + b_3 X^2 + b_4 X^3 + b_5 Y + \\ b_6 Z + b_7 XY + b_8 XZ \\ c_1 + c_2 X + c_3 X^2 + c_4 X^3 + c_5 Y + \\ c_6 Z + c_7 XY + c_8 XZ \end{bmatrix} \tag{3}$$

where a_i, b_i, and c_i are polynomial coefficients. By our definition of $\mathbf{r}_i$ and $\mathbf{r}_{il}$, the expression of $\mathbf{r}(\mathbf{X})$ in (3) should satisfy the following conditions.

$$\begin{aligned} &\mathbf{r}\,|_{\mathbf{X}=\mathbf{X}_1} = \mathbf{r}_1, \mathbf{r}\,|_{\mathbf{X}=\mathbf{X}_2} = \mathbf{r}_2 \\ &\tfrac{\partial \mathbf{r}}{\partial X}\,|_{\mathbf{X}=\mathbf{X}_1} = \mathbf{r}_{1X}, \tfrac{\partial \mathbf{r}}{\partial X}\,|_{\mathbf{X}=\mathbf{X}_2} = \mathbf{r}_{2X} \\ &\tfrac{\partial \mathbf{r}}{\partial Y}\,|_{\mathbf{X}=\mathbf{X}_1} = \mathbf{r}_{1Y}, \tfrac{\partial \mathbf{r}}{\partial Y}\,|_{\mathbf{X}=\mathbf{X}_2} = \mathbf{r}_{2Y} \\ &\tfrac{\partial \mathbf{r}}{\partial Z}\,|_{\mathbf{X}=\mathbf{X}_1} = \mathbf{r}_{1Z}, \tfrac{\partial \mathbf{r}}{\partial Z}\,|_{\mathbf{X}=\mathbf{X}_2} = \mathbf{r}_{2Z} \end{aligned} \tag{4}$$

where $\mathbf{X}_1 = [0\ 0\ 0]^T$ and $\mathbf{X}_2 = [L_e\ \ 0\ 0]^T$ are the local coordinates of the two nodes of an element. Substituting (3) into (4), the polynomial coefficients a_i, b_i, and c_i can be solved with the given values of $\mathbf{r}_i$ and $\mathbf{r}_{il}$. Then, the expression of $\mathbf{r}(\mathbf{X})$ can be expressed as

$$\begin{aligned} \mathbf{r}(\mathbf{X}) = &\left(1 - \frac{3X^2}{{L_e}^2} + \frac{2X^3}{{L_e}^3}\right)\mathbf{r}_1 + \left(X - \frac{2X^2}{L_e} + \frac{2X^3}{{L_e}^2}\right)\mathbf{r}_{1X} \\ &+ \left(Y - \frac{XY}{L_e}\right)\mathbf{r}_{1Y} + \left(Z - \frac{XZ}{L_e}\right)\mathbf{r}_{1Z} + \left(\frac{3X^2}{{L_e}^2} - \frac{2X^3}{{L_e}^3}\right)\mathbf{r}_2 \\ &+ \left(-\frac{X^2}{L_e} + \frac{X^3}{{L_e}^2}\right)\mathbf{r}_{2X} + \frac{XY}{L_e}\mathbf{r}_{2Y} + \frac{XZ}{L_e}\mathbf{r}_{2Z}. \end{aligned} \tag{5}$$

Combined with (1) and (2), (5) can be rewritten in the form as

$$\mathbf{r}(\mathbf{X}) = \mathbf{S}(\mathbf{X})\,\mathbf{q}^e \tag{6}$$

where $\mathbf{S}(\mathbf{X})$ is a 3×24 matrix defined in (7), denoting $\mathbf{I}$ as a third-order identity matrix.

$$\mathbf{S}(\mathbf{X}) = [s_1 \mathbf{I} s_2 \mathbf{I} \ldots s_8 \mathbf{I}]$$

$$s_1 = 1 - \frac{3X^2}{{L_e}^2} + \frac{2X^3}{{L_e}^3},\; s_2 = X - \frac{2X^2}{L_e} + \frac{2X^3}{{L_e}^2}$$

$$s_3 = Y - \frac{XY}{L_e},\; s_4 = Z - \frac{XZ}{L_e}$$

$$s_5 = \frac{3X^2}{{L_e}^2} - \frac{2X^3}{{L_e}^3},\; s_6 = -\frac{X^2}{L_e} + \frac{X^3}{{L_e}^2}$$

$$s_7 = \frac{XY}{L_e}, s_8 = \frac{XZ}{L_e}. \tag{7}$$

Equation (6) represents the position of arbitrary points within the element after displacement, which can also be used to derive the expression of local deformation. Differentiating (6) with respect to the local spatial coordinates, the 3×3 deformation gradient matrix can be expressed as

$$\mathbf{J}\left(\mathbf{X}\right) = \left[\, \frac{\partial \mathbf{r}}{\partial X}\ \frac{\partial \mathbf{r}}{\partial Y}\ \frac{\partial \mathbf{r}}{\partial Z} \,\right]. \tag{8}$$

Remark: The accuracy of the representation for the displacement field in (6) generally depends on the node density. In addition, another solution to improve the accuracy for ANCF is to add the high-order derivative of the position to the absolute nodal coordinates, as described in [47].

Based on (8), the strain distribution on the element can be expressed as (taking the form of Green strain tensor [52])

$$\boldsymbol{\varepsilon}_G\left(\mathbf{X}\right) = \frac{1}{2}\left(\mathbf{J}^T\left(\mathbf{X}\right)\mathbf{J}\left(\mathbf{X}\right) - \mathbf{I}\right). \tag{9}$$

Hence both the global configuration and the local deformation of the soft actuators can be completely described by the absolute coordinates of all the predefined nodes. Without losing generality, such parameterization can also be applied for the description of rotation. With the expression of the deformation gradient in (8), right polar decomposition can be applied to obtain the rotation matrix $\mathbf{R}(\mathbf{X})$ [52], i.e.,

$$\mathbf{J}\left(\mathbf{X}\right) = \mathbf{R}\left(\mathbf{X}\right) \cdot \mathbf{U}\left(\mathbf{X}\right) \tag{10}$$

where $\mathbf{U}(\mathbf{X})$ is called the right stretch matrix. Typically, if the shearing and deformation of the cross section are neglected, $\mathbf{U}(\mathbf{X})$ can be expressed by

$$\mathbf{U}\left(\mathbf{X}\right) = \begin{bmatrix} \lambda_X\left(\mathbf{X}\right) & 0 & 0 \\ 0 & 1 & 0 \\ 0 & 0 & 1 \end{bmatrix} \tag{11}$$

where $\lambda_X(\mathbf{X})$ is the axial stretch ratio of the material in the material coordinate $\mathbf{X}$. Substituting (8) and (11) into (10), $\mathbf{R}(\mathbf{X})$ can be expressed by

$$\mathbf{R}\left(\mathbf{X}\right) = \left[\, \lambda_X(\mathbf{X})^{-1} \cdot \frac{\partial \mathbf{r}}{\partial X}\ \frac{\partial \mathbf{r}}{\partial Y}\ \frac{\partial \mathbf{r}}{\partial Z} \,\right]. \tag{12}$$

According to the orthogonality of $\mathbf{R}(\mathbf{X})$, the orientation of the actuator's centerline can be thus be obtained as

$$\mathbf{R}(X) = \left[\, \frac{\partial \mathbf{r}}{\partial Y} \times \frac{\partial \mathbf{r}}{\partial Z}\ \frac{\partial \mathbf{r}}{\partial Y}\ \frac{\partial \mathbf{r}}{\partial Z} \,\right]|_{Y=Z=0}. \tag{13}$$

With the parameterization of the element motions, geometrical constraints should be further introduced, considering that the actuators are connected to the base stage and the output stage. For the nodes defined at the base stage, their absolute coordinates $\mathbf{q}_b$ can be regarded as constant vectors. For the nodes defined at the output stage, their absolute coordinates $\mathbf{q}_c$ can be determined with the position and orientation of the output stage $\mathbf{x}_o = [\, \mathbf{p}_o{}^T\ \boldsymbol{\theta}_o{}^T \,]^T$. Hence, the whole configuration variables of the robot can be expressed as

$$\mathbf{q} \in \mathbb{R}^{12N_e+6} = \left[\, \mathbf{q}_w{}^T\ \mathbf{x}_o{}^T \,\right]^T \tag{14}$$

where $\mathbf{q}_w$ represents the absolute coordinates of all the N_e nodes that are not defined at the two ends of the actuator.

C. Force Analysis

The motions of the soft parallel robot are generated by the effects of actuation forces, elasticity forces, and external forces, simultaneously. In order to establish the kinematic model for the whole robot with the adopted parametrization method based on ANCF, the generalized forces corresponding to these effects on each element are analyzed. Then, the external-force-dependent kinematic mappings of the soft parallel robot are presented.

1) Actuation Force: For the soft pneumatic actuator, the motion is actuated by the compressed air in the chamber. Denoting P as the input pressure, the virtual work done by the compressed air in an element can be written as

$$\delta W_A = P\delta V_c \tag{15}$$

where δV_c denotes the virtual volume increment of the chamber. With the deformation gradient defined in (8), δV_c can be calculated by

$$\delta V = \frac{\partial\left(\int_{V_c}(|\mathbf{J}\left(\mathbf{X}\right)| - 1)dV\right)}{\partial \mathbf{q}^e}\delta\mathbf{q}^e. \tag{16}$$

Combining with (16), (15) can be rewritten as

$$\delta W_A = \left(\mathbf{Q}_A^e\right)^T \delta\mathbf{q}^e \tag{17}$$

where $\mathbf{Q}_A^e$ is called as the generalized actuation force vector of the element, which can be expressed by

$$\mathbf{Q}_A^e = P\frac{\partial\left(\int_{V_c}(|\mathbf{J}\left(\mathbf{X}\right)| - 1)dV\right)}{\partial \mathbf{q}^e}. \tag{18}$$

It should be noted that, for the actuator in our design, the compressed air produces elongation in the axial direction. For simplification, the element length L_e can be regarded as the function of the input pressure

$$L_e(P) = \lambda(P)L_0 \tag{19}$$

where L_0 and λ represent the initial length of the element and the stretch ratio of the actuator, respectively. Fig. 6 shows the testing results of the relation between the input pressure and the output stretch ratio of three fabricated actuators.

2) Elastic Force: The generalized elastic force acted on an element can be calculated by

$$\mathbf{Q}_E^e = -\frac{\partial U^e\left(\mathbf{q}^e\right)}{\partial \mathbf{q}^e} \tag{20}$$

where U^e is the total elastic potential energy of the element. In general, U^e can be obtained by the volume integration of the elastic energy density $\varphi(\mathbf{X})$, i.e.,

$$U^e = \int_V \varphi\left(\mathbf{X}\right)dV. \tag{21}$$

The calculation of $\varphi(\mathbf{X})$ depends on the adopted constitutive law of materials. For the simulation in this work, to improve the computational efficiency, the linear constitutive law of Euler–Bernoulli beam and 1-D integration is used to calculate (21) for proof-of-concept testing, where the shearing and the deformation of the actuator's cross section are neglected. This

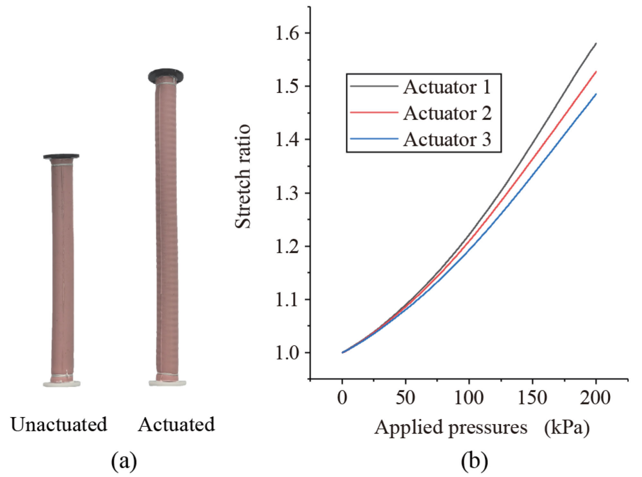

Fig. 6. Actuation tests of the fabricated actuators. (a) Elongation deformation occurs when inflating the chamber of the fiber-reinforced actuator. (b) Relation between the stretch ratio and input pressures is tested for three fabricated actuators.

assumption introduces constraints for the absolute nodal coordinates of elements. Actually, on the two nodes of an element, the deformation gradient can be written as

$$\begin{aligned} \mathbf{G}_1 &= \tfrac{\partial \mathbf{r}}{\partial \mathbf{X}}\,|_{X=Y=Z=0} = \left[\mathbf{g}_{11}\ \mathbf{g}_{12}\ \mathbf{g}_{13}\right] \\ \mathbf{G}_2 &= \tfrac{\partial \mathbf{r}}{\partial \mathbf{X}}\,|_{X=L_e,Y=Z=0} = \left[\mathbf{g}_{21}\ \mathbf{g}_{22}\ \mathbf{g}_{23}\right]. \end{aligned} \tag{22}$$

According to (22), $\mathbf{g}_{i1}$, $\mathbf{g}_{i2}$, and $\mathbf{g}_{i3}$ $(i = 1, 2)$ are parallel to the three basis vectors of the local coordinate system $(O - XYZ)$, respectively. Hence, if there is no deformation of the cross section, $\mathbf{g}_{i2}$ and $\mathbf{g}_{i3}$ are unit orthogonal vectors. Further, if there is no shearing, $\mathbf{g}_{i1}$ will be a unit vector perpendicular to $\mathbf{g}_{i2}$ and $\mathbf{g}_{i3}$. Therefore, $\mathbf{G}_1$ and $\mathbf{G}_2$ are orthogonal matrices. Then, following constraint equations should be satisfied:

$$\begin{aligned} &\mathbf{g}_{ij}^T\mathbf{g}_{ij} = 1\,(i = 1, 2, j = 1, 2, 3) \\ &\mathbf{g}_{ij}{}^T\mathbf{g}_{ik} = 0\,(i = 1, 2, j = 1, 2, 3, j \neq k) \\ &\mathbf{g}_{i1} \times \mathbf{g}_{i2} = \mathbf{g}_{i3}\,(i = 1, 2)\,. \end{aligned} \tag{23}$$

The aforementioned equations can be rewritten in the following vector form

$$\begin{aligned} \mathbf{F}_{ec} = \big[&\mathbf{g}_{12}{}^T\mathbf{g}_{12} - 1\ \mathbf{g}_{13}{}^T\mathbf{g}_{13} - 1\ \mathbf{g}_{12}{}^T\mathbf{g}_{13} \\ &(\mathbf{g}_{12} \times \mathbf{g}_{13} - \mathbf{g}_{11})^T\ \mathbf{g}_{22}{}^T\mathbf{g}_{22} - 1\ \mathbf{g}_{23}{}^T\mathbf{g}_{23} - 1 \\ &\mathbf{g}_{22}{}^T\mathbf{g}_{23}\ (\mathbf{g}_{22} \times \mathbf{g}_{23} - \mathbf{g}_{21})^T\big]^T = \mathbf{0} \end{aligned} \tag{24}$$

Then, considering the deformation of the element's centerline, each component of the curvature can be calculated by

$$\begin{bmatrix} 0 & -k_{b2}(X) & k_{b1}(X) \\ k_{b2}(X) & 0 & -k_t(X) \\ -k_{b1}(X) & k_t(X) & 0 \end{bmatrix} = \mathbf{R}(X)^T \frac{\partial \mathbf{R}(X)}{\partial X} \tag{25}$$

where k_t is the torsion curvature, while k_{b1} and k_{b2} are two orthogonal components of bending curvatures. Besides, the resultant bending curvature and tensile strain (not including the

Algorithm 1: Equation Solver.

Input: Generalized loads $\mathbf{u}$ and initialized $\mathbf{v}_0$.
Output: Indeterminate variables $\mathbf{v}$.

Generating an incremental sequence $\{\mathbf{u}_i | i = 1, 2, \ldots m\}$, where $\mathbf{u}_m = \mathbf{u}$.
$\mathbf{v} \leftarrow \mathbf{v}_0$.
for $i = 1; i \leq m; i++$ **do**
  $\mathbf{Q}_{\text{current}} \leftarrow \tilde{\mathbf{Q}}(\mathbf{u}_i, \mathbf{v})$.
  while $\|\mathbf{Q}_{\text{current}}\| > \varepsilon$ (the precision criterion)**do**
    $\mathbf{J}_v \leftarrow$ Calculating $\mathbf{J}_v$ defined in (35).
    $\mathbf{v} \leftarrow \mathbf{v} - \mathbf{J}_v{}^{-1}\mathbf{Q}_{\text{current}}$.
    $\mathbf{Q}_{\text{current}} \leftarrow \tilde{\mathbf{Q}}(\mathbf{u}_i, \mathbf{v})$.
  end while
end for
Return $\mathbf{v}$.

part caused by actuation) of the centerline can be expressed as

$$\begin{aligned} k_b(X) &= \left(\frac{\partial^2 \mathbf{r}^T}{\partial X^2}\frac{\partial^2 \mathbf{r}}{\partial X^2}\right)^{1/2} |_{Y=Z=0} \\ \varepsilon(X) &= \frac{1}{2}\left(\frac{\partial \mathbf{r}^T}{\partial X}\frac{\partial \mathbf{r}}{\partial X} - 1\right) |_{Y=Z=0}. \end{aligned} \tag{26}$$

Hence, adopting the linear constitutive law, (21) can be calculated by

$$\begin{aligned} U^e = \frac{1}{2}\int_0^{L_e} &\left[EIk_b(X)^2 + GIk_t(X)^2 + EA\varepsilon(X)^2\right. \\ &\left. + \alpha \mathbf{F}_{ec}{}^T\mathbf{F}_{ec}\right] dX \end{aligned} \tag{27}$$

where EI, GI, EA, and α represent the flexural rigidity, the torsion rigidity, the tensile rigidity, and the penalty factor, respectively.

Remark: The effect of actuation is considered in the element's length by (19), which makes the extra tensile strain defined in (26) small. Therefore, the linear constitutive law in (27) can be used to improve the computational efficiency.

3) External Forces: The external forces acted on an element include the payload and the gravity, which can be modeled as a spatially distributed force function $\mathbf{f}^e(\mathbf{X})$. The virtual work due to the external forces can be calculated by

$$\delta W_F = \int_V \mathbf{f}^e(\mathbf{X})^T \delta\mathbf{r}(\mathbf{X})\,dV. \tag{28}$$

Substituting (6) into (28), the corresponding generalized force vector of the external forces can be expressed by

$$\mathbf{Q}_F^e = \int_V \mathbf{S}(\mathbf{X})^T \mathbf{f}^e(\mathbf{X})\,dV. \tag{29}$$

Considering the actuator in our design, $\mathbf{f}^e(\mathbf{X})$ can be simplified by the force distributed along the center line $\mathbf{f}_L^e(X)$. Hence, (29) can be rewritten as

$$\mathbf{Q}_F^e = \int_0^{L_e} \mathbf{S}(\left[X\ 0\ 0\right])^T \mathbf{f}_L^e(X)\,dX. \tag{30}$$

Algorithm 2: ForwardKinematics.

Input: Input pressures $\mathbf{P}$ and payloads $\mathbf{f}$.
Output: Configuration parameters $\mathbf{q}$ of the robot.

1: $\boldsymbol{\lambda} \leftarrow$ Calculate the stretch ratio of each actuator according to $\mathbf{P}$.
2: $\mathbf{u} \leftarrow [\boldsymbol{\lambda}^T\ \mathbf{f}^T]^T$.
3: $\mathbf{v}_0 \leftarrow$ Initialize the value of $\mathbf{q}$.
4: $\mathbf{v} \leftarrow \mathrm{EquationSolver}(\mathbf{u}, \mathbf{v}_0)$
5: **Return** $\mathbf{q} \leftarrow \mathbf{v}$.

Algorithm 3: InverseKinematics.

Input: Desired output position $\mathbf{p}_o$ and payloads $\mathbf{f}$.
Output: Pressures $\mathbf{P}$ and configuration parameters $\mathbf{q}$.

1: $\mathbf{u} \leftarrow [\mathbf{p}_o{}^T\ \mathbf{f}^T]^T$.
2: Initialize the values of $\boldsymbol{\lambda}$ and $[\mathbf{q}_w{}^T\ \boldsymbol{\theta}_o{}^T]^T$.
3: $\mathbf{v}_0 \leftarrow [\mathbf{q}_w{}^T\ \boldsymbol{\theta}_o{}^T\ \boldsymbol{\lambda}^T]^T$.
4: $\mathbf{v} \leftarrow \mathrm{EquationSolver}(\mathbf{u}, \mathbf{v}_0)$
5: $[\mathbf{q}_w{}^T\ \boldsymbol{\theta}_o{}^T\ \boldsymbol{\lambda}^T]^T \leftarrow \mathbf{v}$
6: $\mathbf{q} \leftarrow [\mathbf{p}_w{}^T\ \mathbf{p}_o{}^T\ \boldsymbol{\theta}_o{}^T]^T$
7: $\mathbf{P} \leftarrow$ Calculating input pressures of each actuator according to $\boldsymbol{\lambda}$.
8: **Return** $\mathbf{P}$ and $\mathbf{q}$.

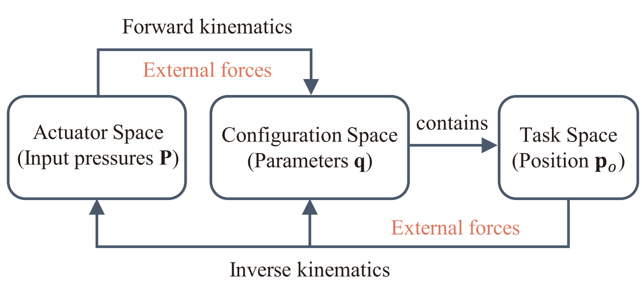

Fig. 7. Schematic illustration of the mappings among the kinematic spaces of the soft parallel robot.

D. Kinematic Mappings

With the results of force analysis, the total generalized force acted on an element can be calculated by

$$\mathbf{Q}^e = \mathbf{Q}^e_A + \mathbf{Q}^e_E + \mathbf{Q}^e_F. \tag{31}$$

Then, the generalized force $\mathbf{Q} \in \mathbb{R}^{12N_e+6}$ with respect to the global configuration parameter $\mathbf{q}$ of the robot can be assembled by $\mathbf{Q}^e$. Considering the equilibrium condition, the following equation should be satisfied:

$$\mathbf{Q}\left(\mathbf{q}, \boldsymbol{\lambda}\left(\mathbf{P}\right), \mathbf{f}\right) = \mathbf{0} \tag{32}$$

where $\boldsymbol{\lambda} \in \mathbb{R}^3$ is a vector representing the stretch ratios of all the actuators, and $\mathbf{f} \in \mathbb{R}^3$ represents the external force acted on the output stage. Therefore, (32) describes the relation among the input pressures of the actuators $\mathbf{P}$, the robot configuration $\mathbf{q}$, and the external payloads $\mathbf{f}$.

Based on (32), both the forward and inverse kinematics analysis (as illustrated in Fig. 7) can be achieved by a unified method as follow. First, divide the variables in (32) into two parts, i.e., the given generalized loads $\mathbf{u}$ and the indeterminate variables $\mathbf{v}$. As for the forward and inverse kinematics, $\mathbf{u} \in \mathbb{R}^6$ and $\mathbf{v} \in \mathbb{R}^{12N_e+6}$ are defined in (33) and (34), respectively.

$$\mathbf{u} = \left[\boldsymbol{\lambda}(\mathbf{P})^T\ \mathbf{f}^T\right]^T, \mathbf{v} = \mathbf{q} \tag{33}$$

$$\mathbf{u} = \left[\mathbf{p}_o{}^T\ \mathbf{f}^T\right]^T, \mathbf{v} = \left[\mathbf{q}_w{}^T\ \boldsymbol{\theta}_o{}^T\ \boldsymbol{\lambda}(\mathbf{P})^T\right]^T. \tag{34}$$

Then, (32) can be rewritten as $\tilde{\mathbf{Q}}(\mathbf{u}, \mathbf{v}) = \mathbf{0}$. In order to solve the indeterminate variables with the given $\mathbf{u}$ and ensure the convergence, $\mathbf{u}$ can be divided into a series of increment steps. In each step where $\mathbf{u} = \mathbf{u}_i$, the Newton–Raphson method [53] can be used to update $\mathbf{v}$ with the following iterative form:

$$\begin{aligned} &\mathbf{v}_{j+1} = \mathbf{v}_j - \mathbf{J}_v{}^{-1}\big|_{\mathbf{v}=\mathbf{v}_j,\mathbf{u}=\mathbf{u}_i}\ \tilde{\mathbf{Q}}\left(\mathbf{u}_i, \mathbf{v}_j\right) \\ &\text{where}\quad \mathbf{J}_v \in \mathbb{R}^{(12N_e+6)\times(12N_e+6)} = \frac{\partial\tilde{\mathbf{Q}}(\mathbf{u},\mathbf{v})}{\partial\mathbf{v}}. \end{aligned} \tag{35}$$

The iterative processes in each step should stop when the norm of $\tilde{\mathbf{Q}}$ is within the criterion value. The detailed procedures for obtaining the results of $\mathbf{v}$ are also presented in Algorithm 1. In addition, the forward and inverse kinematics based on this method are summarized in Algorithms 2 and 3, respectively.

IV. Simulation and Experimental Results

To evaluate the developed kinematic model, simulations and experiments are conducted on the workspace analysis, stiffness analysis, and feedforward control of the soft parallel robot.

A. Parameter Definition

In order to validate our developed model on the soft parallel robot, several actuator-specific and actuator-independent parameters should be first given, including the flexural rigidity, the torsion rigidity, the tensile rigidity, the element number for each actuator, and the penalty factor. Among them, the flexural rigidity of the actuator $EI = 0.0025\ \mathrm{N}\cdot\mathrm{m}^2$ is identified by a set of horizontal loading tests, as described in [48]. According to the symmetry of the actuator, the torsion rigidity $GI = 0.0016\ \mathrm{N}\cdot\mathrm{m}^2$ can be determined by $2EI/3$. While $EA = 68.4\ \mathrm{N}$ is calculated according to the Young's modulus of the used rubber (ELASTOSIL M4601, $E = 483.5$ kPa [54]).

Additionally, there are two parameters needed to be determined, i.e., the element number n_e of each actuator, and the penalty factor α. In general, a larger number of elements can improve the model's accuracy, which, however, will result in larger computation cost as well. To choose a suitable element number n_e for each actuator, the relations among n_e, computation cost, and the simulation results should be considered. First, we denote $\mathbf{x}^o_n$ as the predicted position of the output stage (in the unactuated state) when $n_e = n$. Then, we can express a variation of the prediction result (when n_e is increased by 1) as $\Delta\mathbf{x}^o_n = \mathbf{x}^o_{n+1} - \mathbf{x}^o_n$, which can be used to evaluate the sensitivity of $\mathbf{x}^o_n$ to the element number. As shown in Fig. 8(a), $\Delta\mathbf{x}^o_n$, and calculation time are plotted as functions of the element number. The results demonstrate that $\|\Delta\mathbf{x}^o_n\|$ is close to zero when $n_e > 4$. Hence, for the tradeoff between the computational efficiency and model accuracy, we choose n_e as 5 in this work.

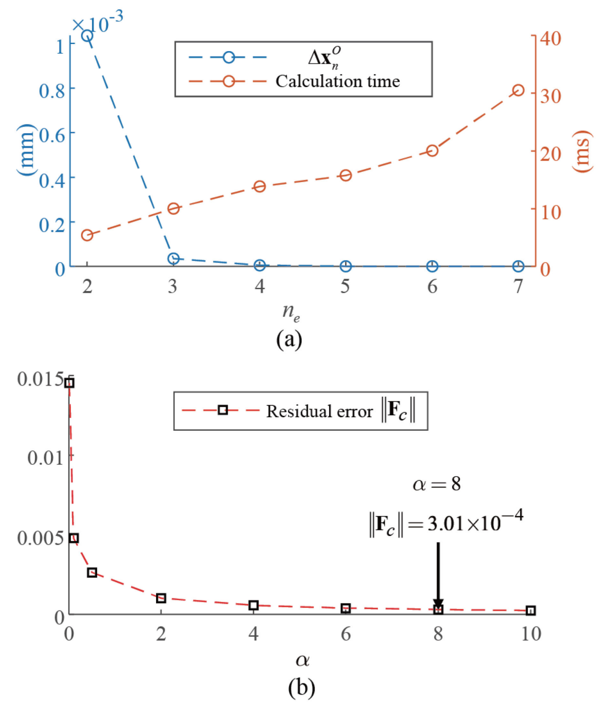

Fig. 8. Numerical analysis on the influence of n_e and α. (a) Relations among n_e, the sensitivity of the predicted $\mathbf{x}_n^o$ to the element number, and the calculation time. (b) Relation between the penalty factor α and the residual error of constraint equations.

Besides, a larger value of the penalty factor α can make the simulation result better satisfy the given constraint conditions. However, a too large value of α may influence the convergence of the kinematic algorithms. To evaluate the effect of this parameter, we first define the global constraint equations $\mathbf{F}_c = \mathbf{0}$ (which can be obtained by merging the constraint equations of all the elements). Then, the relation between α and $\|\mathbf{F}_c\|$ can be calculated out. The obtained result is shown in Fig. 8(b), which illustrates that $\|\mathbf{F}_c\|$ is close to zero when $\alpha = 8$. In addition, it is verified by numerical tests that this choice of α can contribute to the convergence of the proposed algorithms.

B. Experimental Setup

To regulate the input pressures for the robot, electronic pressure regulators (QB1XANEEN100P400KPG, Proportion-Air) and the control module (MicroLabBox-DS1202, dSPACE) are used. The control commands are sent by MATLAB (interacting with the control module by the serial port), where the kinematic calculation is implemented. In addition, a camera system (Optitrack, Prime 13) is configured to capture the robot's motion.

C. Workspace Analysis

With the developed kinematic model, we analyze the positional and orientational workspace of the designed soft parallel robot. In order to avoid damage of soft actuators, the maximum value of the applied pressure is set as $P_{\max} = 180$ kPa according to prior experimental results. Then, the Monte Carlo simulation is used to obtain the workspace with the kinematic model. To this end, we first generate a $3 \times n_s$ random matrix $\mathbf{P}_{\text{sam}}$, where we manually set n_s as 5000. Each element of this matrix ${P_{\text{sam}}}^{ij}$ $(i = 1, 2, 3, j = 1, 2, \ldots n_s)$ is a uniformly distributed random number from 0 to $P_{\max}$. For each integer i from 1 to n_s, setting the pressure vector $\mathbf{P}$ as $[\,{P_{\text{sam}}}^{1j}\ {P_{\text{sam}}}^{2j}\ {P_{\text{sam}}}^{3j}\,]^T$, calculate the robot pose with our developed model and record the result. Finally, we obtain n_s robot poses within its workspace.

Fig. 9(a) and (b) shows the simulation result of the positional and orientational workspace of the robot. To verify the calculation result by experiments, we actuate the robot with different input pressures and record the robot poses. The detailed actuation schemes are as follows.

1) Inflate each actuator gradually (with the input pressure from 0 kPa to $P_{\max}$), meanwhile, the input pressures of other two actuators are fixed by the extreme values (0 kPa or $P_{\max}$).
2) Pairs of the actuators are inflated gradually together (with the input pressure from 0 kPa to $P_{\max}$), and the remained one is applied with the extreme input pressure (0 kPa or $P_{\max}$).

Testing the aforementioned total 18 actuation schemes, the position and orientation of the output stage can be captured, which are compared with the model prediction [as shown in Fig. 9(c) and (d)]. The average and maximum position errors are 0.98 and 2.05 cm, respectively (about 4.1% and 8.6% of the maximum length of the robot's workspace). The length of the workspace is defined as the maximum positional distance between two points on the experimental boundaries of the workspace. Besides, the average and maximum orientation errors are 5.85 ° and 12.88 °, respectively. Fig. 9(e) and (f) shows the error distributions at different robot poses. In addition, the average time cost for motion prediction with given input pressures in each step is about 2.6 ms. It should be noted that, due to the fabrication errors, the mechanical properties of the three actuators are not same. For example, as shown in Fig. 6, three actuators of the soft robot have different actuation-elongation relations. Such differences among actuators may cause the asymmetry of the error distributions shown in Fig. 9(e) and (f).

Remark: We may mention that the observed modeling errors may be also resulted from several factors, such as the cross-sectional deformation, the existence of shearing, and the rigidity change of the actuator during inflation. In this work, these factors are not taken into consideration to achieve a more computationally efficient implementation. It is worthy of mentioning that we can extend our model to further consider the more general 3-D deformation including the shearing and the deformation of the cross section, by substituting the spatial strain tensor in (9) into a nonlinear constitutive law defined by the expression of the strain energy density $\varphi(\mathbf{X})$ to calculate the overall strain energy in (21).

D. Comparisons With the Conventional FEM

To further demonstrate the accuracy and computational efficiency of our developed model, we construct a 3-D FEM model for comparison. In this sense, we adopt the FEM modeling processes for fiber-reinforced actuators with ABAQUS/Standard

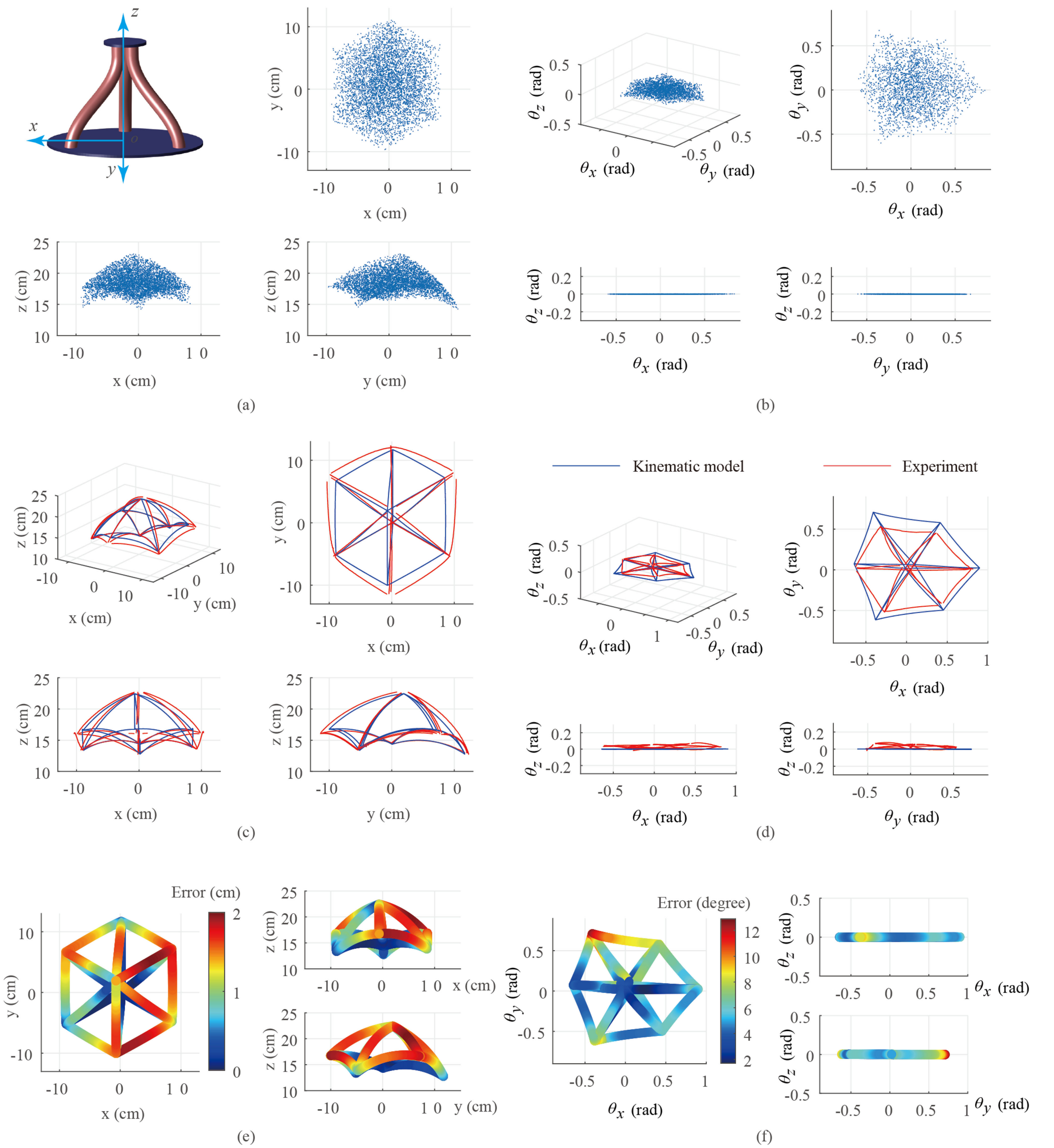

Fig. 9. Workspace analysis of the soft parallel robot. (a) Position workspace and (b) orientation workspace of the robot are calculated out with Monte Carlo simulation based on our kinematic model. The simulated boundaries of the robot's workspace are compared with the experimental results (c) and (d). (e) and (f) Prediction error distributions of both the position and orientation are shown.

(Simulia, Dassault Systemes). In this model, the material behavior of the silicone rubber (ELASTOSIL M4601) is characterized by a hyperelastic incompressible Yeoh model ($C_1 = 0.11$ MPa and $C_2 = 0.02$ MPa) [48], while the fiber is modeled as linear elastic material (with Young's modulus of 2.9 GPa and Poisson's ratio of 0.41). Quadratic tetrahedron hybrid elements (type C3D10H in Abaqus) and linear beam elements (type B31 in Abaqus) are used to discrete the silicone rubber and the fiber of actuators, respectively. Tie constraints are set between the fiber and the silicone rubber tube, also, between actuators and the output stage (which is modeled by a discrete rigid body). The effect of compressed air is modeled

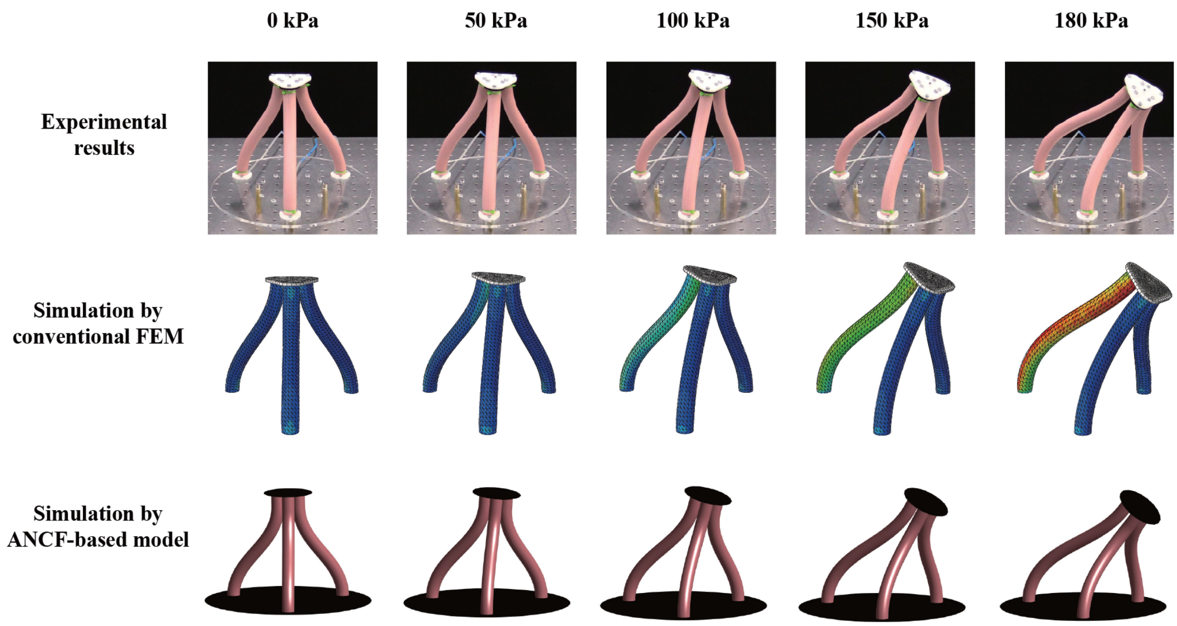

Fig. 10. Illustrations of the simulated configurations of the soft parallel robot with the FEM and our ANCF-based model as well as the experimental results, when one of the actuators is actuated. The top row shows the experimental results. The middle and bottom rows show the simulation results by the conventional FEM and the ANCF-based kinematic model, respectively.

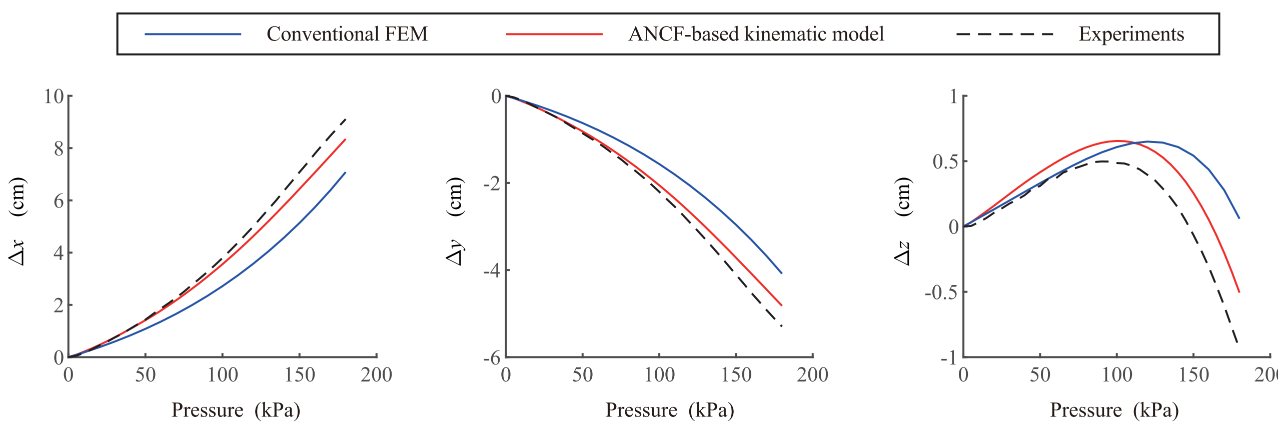

Fig. 11. Comparisons of the displacements of the output stage calculated by the conventional FEM and the ANCF-based kinematic model as well as the experimental results.

by uniformly distributed pressures acted on the internal walls of the actuators. In addition, the gravity of the whole system is also considered. Then, we use the constructed FEM model to predict the robot motion when actuating one of the actuators with the input pressure from 0 to 180 kPa. The predicted evolution of the robot configuration is shown in Fig. 10, which is compared with the simulation results by the ANCF-based kinematic model. It can be found that the results of the two models are both well-matched with the experiments. The FEM model takes 7.3 min to simulate the whole processes, while the time cost of our developed kinematic model is only 15 ms. Furthermore, our kinematic model is more accurate in predicting the positions of the output stage, which is illustrated in Fig. 11. The main reason may be that the FEM model cannot consider the uncertainty of fabrication errors of the soft actuators. For example, the three actuators of the soft robot have different actuation-elongation relations, which is difficult to be handled in the standard FEM modeling processes. However, such differences of actuator properties are considered in our model by fitting the relation between the stretch ratios and input pressures [as expressed in (19)] with experimental data.

E. Stiffness Analysis

The robot stiffness can be analyzed with the displacements resulted from loadings in different directions [as shown in Fig. 12(a)]. In this work, the influence of the design parameter ϕ (as illustrated in Fig. 3) on the robot stiffness is investigated.

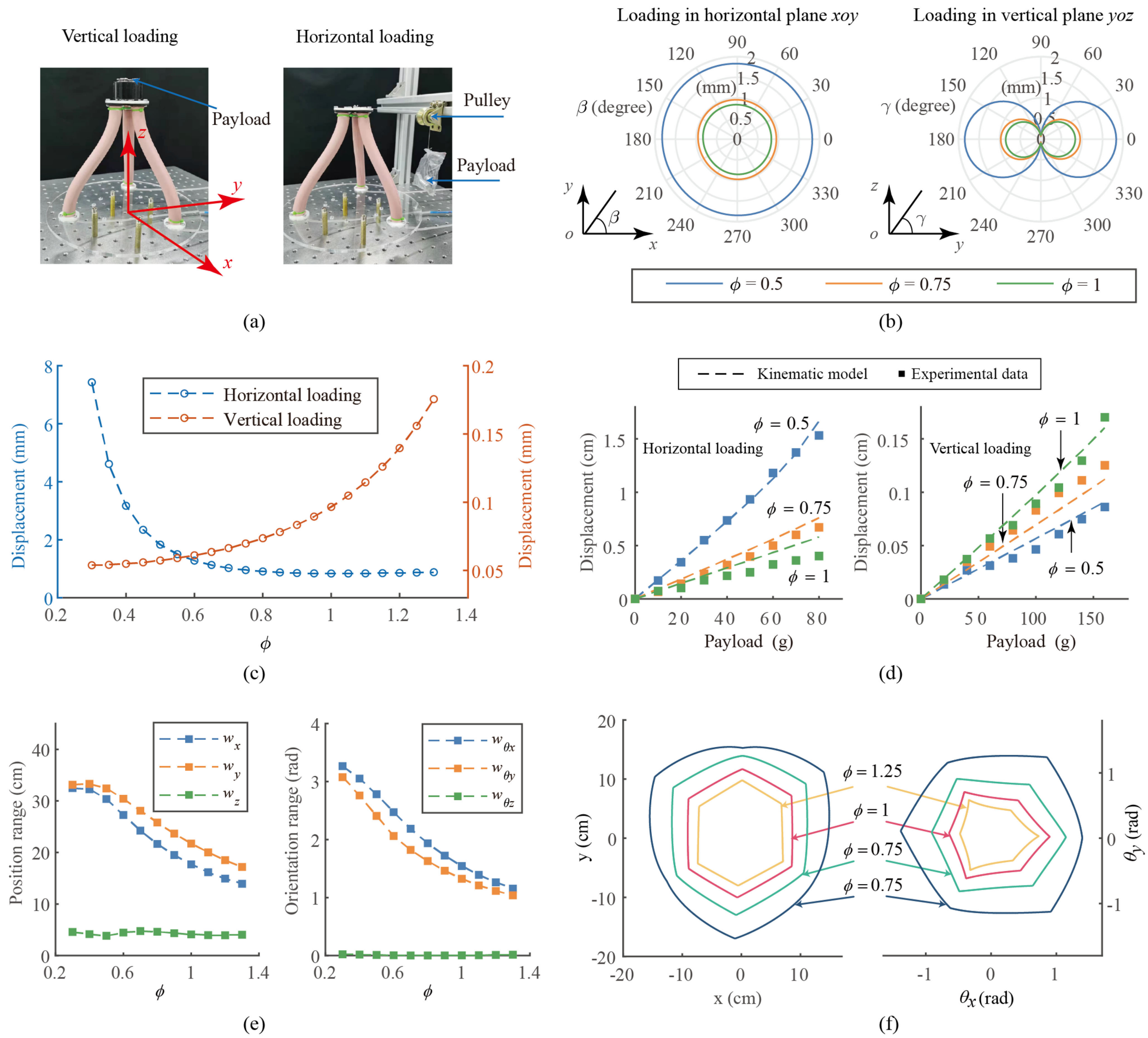

Fig. 12. Stiffness analysis of the soft parallel robot. (a) Output stage of the soft parallel robot is subjected to external payloads. (b) Displacements of the output stage when subjected to a constant load of 0.1 N in different directions, which are simulated with different values of ϕ. (c) With the constant load of 0.1 N in horizontal ($\beta = 90^\circ$) and vertical ($\gamma = -90^\circ$) directions, the relation between the parameter ϕ and the robot displacement is simulated. (d) For the robot with different values of ϕ, the experimental and simulated results of payload-displacement relations are compared. (e) (Left) Simulated ranges of position and (right) orientation workspaces are shown. (f) Shapes of the workspace boundaries of the soft parallel robot with different values of ϕ.

To this end, with different values of ϕ, we firstly analyze the displacements of the output stage when subjected to a constant load of 0.1 N in different directions by simulation, where the result is shown in Fig. 12(b). It can be found that the stiffness of the robot in all the horizontal directions is almost uniformed and much lower than the vertical stiffness. In order to further investigate the influence of ϕ to the stiffness quantitatively, we choose two specific loading directions, where $\beta = 90^\circ$ (parallel to horizontal axis y) and $\gamma = -90^\circ$ (parallel to the vertical axis $-z$), respectively. Then, the ϕ-displacement relation is simulated in these two loading directions, as shown in Fig. 12(c). The results indicate that, as ϕ increases, the horizontal stiffness will largely increase, in contrast, the vertical stiffness will decrease. In this sense, we carry out experiments with different horizontal and vertical loadings. The experimental results are shown in Fig. 12(d), which agree well with the simulation results. In addition, the enhancement of horizontal stiffness by raising ϕ may come at the cost of the loss of the workspace. In order to investigate this effect, we quantitatively analyze the range of robot workspace when changing ϕ. The simulated ranges of position (w_l ($l = x, y, z$)) and orientation workspaces ($w_{\theta l}$ ($l = x, y, z$)) are shown in Fig. 12(e) and the shapes of the workspace boundaries with different values of ϕ are shown in Fig. 12(f).

F. Feedforward Control

Considering that our soft parallel robot has three actuators, we can either control the 3-DoF translation or rotation of the output stage. However, as demonstrated in Fig. 9(d), the output stage can perform very limited rotation along the vertical axis z. Hence, in this section, we only develop the model-based controller to track the 3-D position of the output stage of the soft parallel robot.

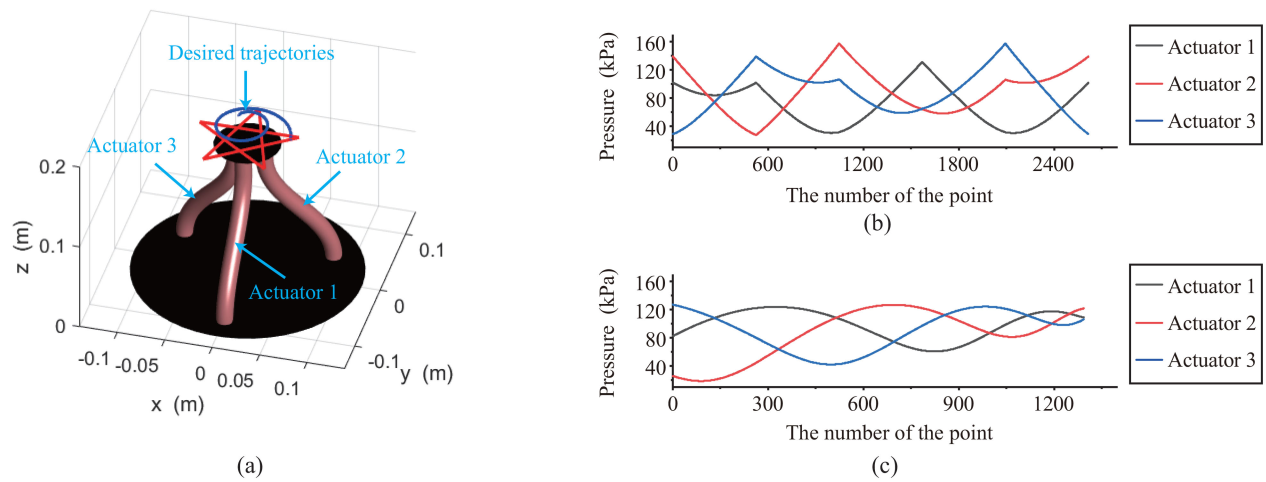

Fig. 13. (a) The desired trajectories defined within the robot workspace. Input pressures of the robot's actuators are calculated out in every discrete point defined along the trajectories of the (b) star and (c) spiral curve.

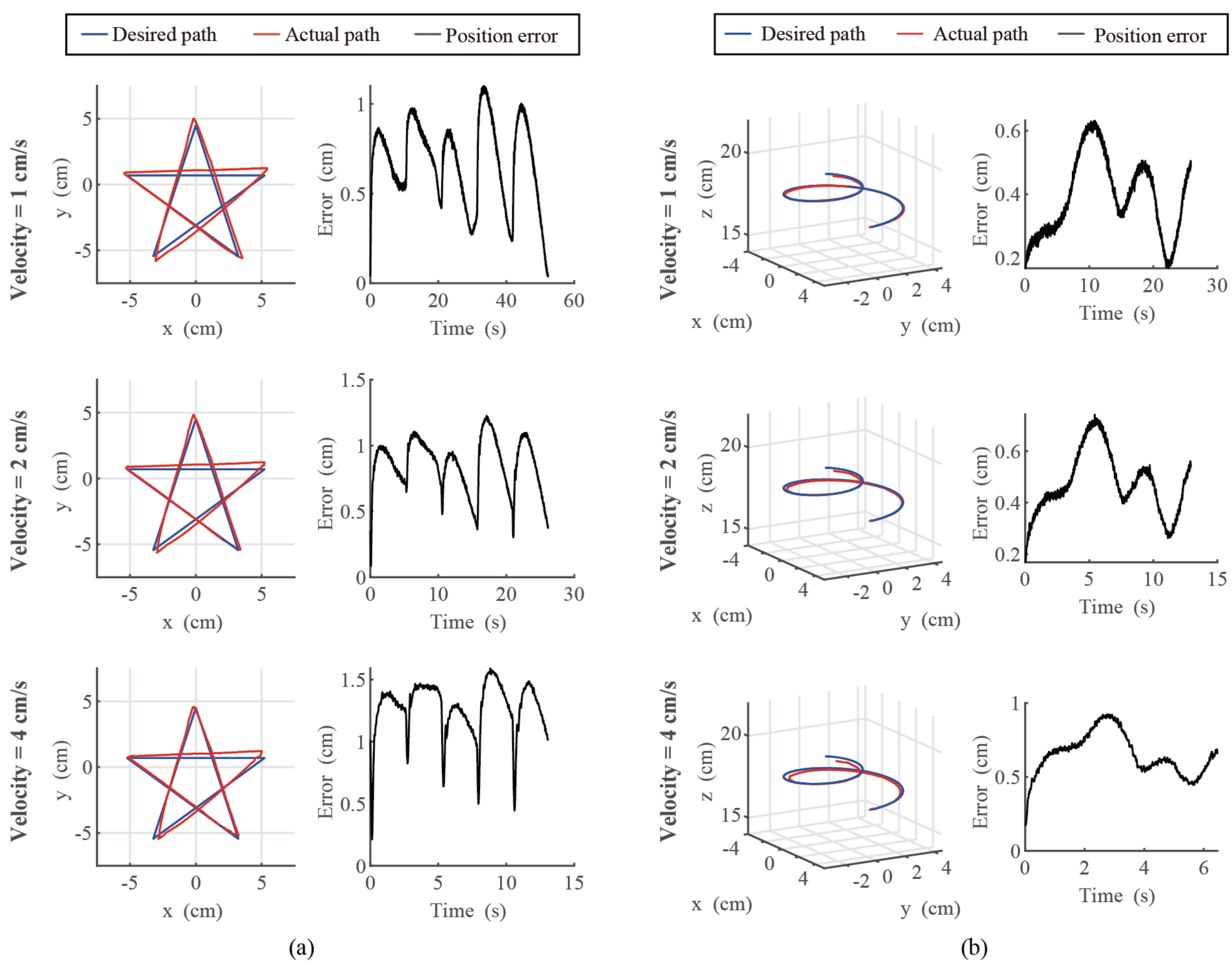

Fig. 14. Experimental results of tracking the trajectory of a (a) star and (b) spiral curve with different output velocities.

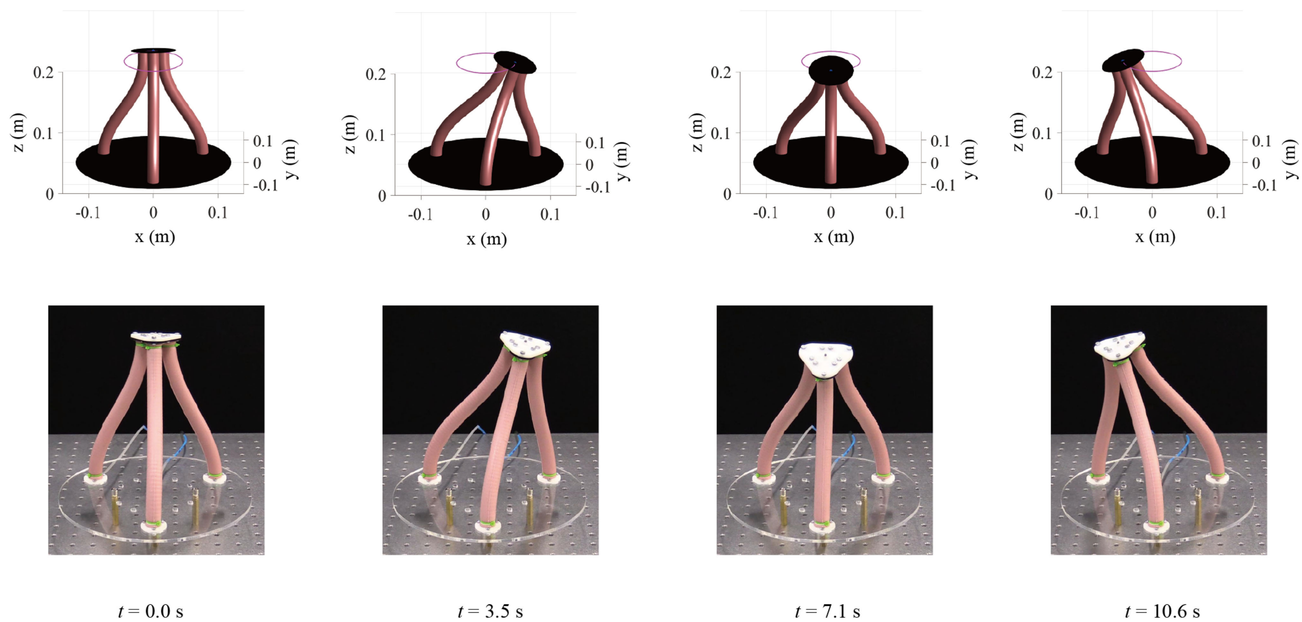

Fig. 15. Comparisons between the simulated configurations (the top row) and the experimental pictures (the bottom row) of the robot when tracking a circular trajectory, where the output velocity is 2 cm/s.

Algorithm 4: Feedforward Trajectory Tracking Controls.

Input: A desired spatial trajectory within the robot's workspace $\varsigma(t)(t \in [0, T_h])$ and payloads $\mathbf{f}$.
Output: The robot is controlled to follow the trajectory tracking motion.

```
Generate a series of sample points
  𝒳^sam = {x_i^sam | i = 1, 2, ..., N} along ς(t)
P, q ← InverseKinematics (x_1^ref, f).
Sending signals to the control module according to P.
t_c ← 0.   // initialize the current time.
while t_c ≤ T_h do
  Find x_d ∈ 𝒳^sam, which minimize ‖x_d − ς(t_c)‖.
  P, q ← InverseKinematics (x_d, f).
  Sending signals to the control module according to
  P.
  t_c ← Update the current time.
end while
```

The inverse kinematics discussed in Section III can be used for the feedforward trajectory tracking control. In general, an arbitrary spatial target trajectory within the robot's workspace can be discretized by a series of points along it. Then, the trajectory tracking motion can be transferred into a sequence of point-to-point motions, where the input pressures for each point are precalculated. The procedure of feedforward trajectory tracking control is presented in Algorithm 4.

To verify the development, we control our fabricated soft parallel robot to follow the trajectories, such as a star and a spiral curve [as shown in Fig. 13(a)]. First, we discretize the trajectories by points with the intervals of 0.2 mm. Then, the input pressures of the robot on each point are calculated [as shown in Fig. 13(b) and (c)]. Finally, the trajectory tracking motions are tested under different output velocities. The experimental results are presented in Fig. 14, where the actual trajectories of the output stage are compared to the desired ones. Denoting $\{\mathbf{x}_i^{\mathrm{act}} | i = 1, 2, \ldots, N\}$ and $\{\mathbf{x}_i^{\mathrm{ref}} | i = 1, 2, \ldots, N\}$ as the captured positions of the output stage during the motions and their referenced values, respectively, the tracking error can be evaluated by the average Euclidean distance:

$$\mathrm{Error} = \frac{1}{N} \sum_{i=1}^{N} \sqrt{\left(\mathbf{x}_i^{\mathrm{ref}} - \mathbf{x}_i^{\mathrm{act}}\right)^T \left(\mathbf{x}_i^{ref} - \mathbf{x}_i^{\mathrm{act}}\right)}. \tag{36}$$

According to (36), the mean tracking errors under the velocity of 1, 2, and 4 cm/s are 0.62, 0.72, and 0.94 cm (about $2.6\% - 3.9\%$ of the maximum length of the workspace), respectively. In addition, the developed model can also well predict the robot shape during the motion, as shown in Fig. 15. We may mention that the average time for calculating the input pressure and the robot's configuration for each target point (with the given intervals) is about 3.5 ms, which makes the developed controller efficient enough for real-time applications. The simulation and experimental results well demonstrate the accuracy and computational efficiency of our developed model and the model-based controller.

Remark: To satisfy the low-speed conditions required in (32), we choose the speed range of 1–4 cm/s in the trajectory tracking test according to the prior experimental results. It can be found that, within such speed range, the tracking error will not rise sharply with the increase of the speed.

V. Conclusion

This article presented a general framework on the design, modeling, characterization, and control of a class of soft parallel robots. Different from the designs of the traditional parallel mechanism, the kinematic chains of the presented robot were entirely soft that consisted of three fiber-reinforced pneumatic actuators. In order to handle the challenges of accurate motion simulation, performance analysis, and control for such 3-D soft mechanisms, a ANCF-based kinematic model was developed. In this model, both the global motion and the local deformation of the soft parallel robot can be well parameterized. Hence, the effects of actuation forces, elasticity, and external forces were completely analyzed, which led to an accurate kinematic mapping between the actuation space and the configuration space. Based on the developed model, the robot workspace and stiffness with different design parameters were well investigated, which were all verified by the experimental results. Finally, a model-based feedforward controller was developed, which performed an average positioning error of $0.62 - 0.94$ cm (about $2.6\% - 3.9\%$ of the maximum length of the robot's workspace) when tracking different trajectories with the output velocity under $1 - 4$ cm/s. The presented model-based controller can also be applied for the tasks of real-time robot manipulation by the interactive interface, which will be considered as our future work.

We may also note that this work mainly focused on the kinematic modeling of 3-D soft mechanisms in low-speed conditions. Some dynamic factors including the external disturbances, however, were not considered in the developed model and the controller design. In the future, we will extend our model for more general dynamic conditions by taking the viscoelasticity of materials and hysteresis of the actuation system into account, and further develop the robust control strategy to handle the external perturbations or disturbances.

References

[1] R. F. Shepherd *et al.*, "Multigait soft robot," *Proc. Nat. Acad. Sci.*, vol. 108, no. 51, pp. 20400–20403, 2011.

[2] A. D. Marchese, R. K. Katzschmann, and D. Rus, "A recipe for soft fluidic elastomer robots," *Soft Robot.*, vol. 2, no. 1, pp. 7–25, 2015.

[3] F. Renda, M. Giorelli, M. Calisti, M. Cianchetti, and C. Laschi, "Dynamic model of a multibending soft robot arm driven by cables," *IEEE Trans. Robot.*, vol. 30, no. 5, pp. 1109–1122, Oct. 2014.

[4] H. Wang, R. Zhang, W. Chen, X. Wang, and R. Pfeifer, "A cable-driven soft robot surgical system for cardiothoracic endoscopic surgery: Preclinical tests in animals," *Surg. Endoscopy*, vol. 31, no. 8, pp. 3152–3158, 2017.

[5] H. Rodrigue, W. Wang, M.-W. Han, T. J. Kim, and S.-H. Ahn, "An overview of shape memory alloy-coupled actuators and robots," *Soft Robot.*, vol. 4, no. 1, pp. 3–15, 2017.

[6] H. Jin, E. Dong, M. Xu, C. Liu, G. Alici, and Y. Jie, "Soft and smart modular structures actuated by shape memory alloy (SMA) wires as tentacles of soft robots," *Smart Mater. Structures*, vol. 25, no. 8, 2016, Art. no. 085026.

[7] G. Gu, J. Zou, R. Zhao, X. Zhao, and X. Zhu, "Soft wall-climbing robots," *Sci. Robot.*, vol. 3, no. 25, 2018, Art. no. eaat2874.

[8] G. Gu, U. Gupta, J. Zhu, L. Zhu, and X. Zhu, "Modeling of viscoelastic electromechanical behavior in a soft dielectric elastomer actuator," *IEEE Trans. Robot.*, vol. 33, no. 5, pp. 1263–1271, Oct. 2017.

[9] C. Majidi, "Soft robotics: A perspective-current trends and prospects for the future," *Soft Robot.*, vol. 1, no. 1, pp. 5–11, 2013.

[10] D. Rus and M. T. Tolley, "Design, fabrication and control of soft robots," *Nature*, vol. 521, no. 7553, pp. 467–75, 2015.

[11] G. Gu *et al.*, "A soft neuroprosthetic hand providing simultaneous myoelectric control and tactile feedback," *Nature Biomed. Eng.*, to be published, doi: 10.1038/s41551-021-00767-0.

[12] A. D. Marchese and D. Rus, "Design, kinematics, and control of a soft spatial fluidic elastomer manipulator," *Int. J. Robot. Res.*, vol. 35, no. 7, pp. 840–869, 2015.

[13] C. Della Santina, R. K. Katzschmann, A. Bicchi, and D. Rus, "Model-based dynamic feedback control of a planar soft robot: Trajectory tracking and interaction with the environment," *Int. J. Robot. Res.*, vol. 39, pp. 490–513, 2020.

[14] V. Falkenhahn, A. Hildebrandt, R. Neumann, and O. Sawodny, "Dynamic control of the bionic handling assistant," *IEEE/ASME Trans. Mechatronics*, vol. 22, no. 1, pp. 6–17, Feb. 2017.

[15] Y. Wei *et al.*, "A novel, variable stiffness robotic gripper based on integrated soft actuating and particle jamming," *Soft Robot.*, vol. 3, no. 3, pp. 134–143, 2016.

[16] J. Merlet, *Parallel Robots*. Berlin, Germany: Springer, 2005.

[17] F. Pierrot, C. Reynaud, and A. Fournier, "Delta: A simple and efficient parallel robot," *Robotica*, vol. 8, no. 2, pp. 105–109, 1990.

[18] P. K. Jamwal, S. Xie, and K. C. Aw, "Kinematic design optimization of a parallel ankle rehabilitation robot using modified genetic algorithm," *Robot. Auton. Syst.*, vol. 57, no. 10, pp. 1018–1027, 2009.

[19] L. Lindenroth *et al.*, "Design of a soft, parallel end-effector applied to robot-guided ultrasound interventions," in *Proc. IEEE/RSJ Int. Conf. Intell. Robots Syst.*, 2017, pp. 3716–3721.

[20] J. B. Hopkins, J. Rivera, C. Kim, and G. Krishnan, "Synthesis and analysis of soft parallel robots comprised of active constraints," *J. Mechanisms Robot.*, vol. 7, no. 1, 2015, Art. no. 011002.

[21] H. Kozuka *et al.*, "A compliant-parallel mechanism with bio-inspired compliant joints for high precision assembly robot," *Procedia CIRP*, vol. 5, pp. 175–178, 2013.

[22] H. Kozuka *et al.*, "A bio-inspired compliant parallel mechanism for high-precision robots," in *Proc. IEEE Int. Conf. Robot. Automat.*, 2012, pp. 3122–3127.

[23] A. A. A. Moghadam, A. Kouzani, K. Torabi, A. Kaynak, and M. Shahinpoor, "Development of a novel soft parallel robot equipped with polymeric artificial muscles," *Smart Mater. Structures*, vol. 24, no. 3, 2015, Art. no. 035017.

[24] M. Garcia, A. A. A. Moghadam, A. Tekes, and R. Emert, "Development of a 3D printed soft parallel robot," in *Proc. ASME Int. Mech. Eng. Congr. Expo.*, 2020, Art. no. V07AT07A008.

[25] L. Lindenroth, R. J. Housden, S. Wang, J. Back, K. Rhode, and H. Liu, "Design and integration of a parallel, soft robotic end-effector for extracorporeal ultrasound," *IEEE Trans. Biomed. Eng.*, vol. 67, no. 8, pp. 2215–2229, Aug. 2020.

[26] Y. Wang and Q. Xu, "Design and testing of a soft parallel robot based on pneumatic artificial muscles for wrist rehabilitation," *Sci. Rep.*, vol. 11, no. 1, 2021, Art. no. 1273.

[27] T. Mahl, A. Hildebrandt, and O. Sawodny, "A variable curvature continuum kinematics for kinematic control of the bionic handling assistant," *IEEE Trans. Robot.*, vol. 30, no. 4, pp. 935–949, Aug. 2014.

[28] I. S. Godage, G. A. Medranocerda, D. T. Branson, E. Guglielmino, and D. G. Caldwell, "Modal kinematics for multisection continuum arms," *Bioinspiration Biomimetics*, vol. 10, no. 3, pp. 035002–035002, 2015.

[29] L. Wang and N. Simaan, "Geometric calibration of continuum robots: Joint space and equilibrium shape deviations," *IEEE Trans. Robot.*, vol. 35, no. 2, pp. 387–402, Apr. 2019.

[30] P. S. Gonthina, A. D. Kapadia, I. S. Godage, and I. D. Walker, "Modeling variable curvature parallel continuum robots using euler curves," in *Proc. Int. Conf. Robot. Automat.*, 2019, pp. 1679–1685.

[31] I. Singh, Y. Amara, A. Melingui, P. Mani Pathak, and R. Merzouki, "Modeling of continuum manipulators using Pythagorean hodograph curves," *Soft Robot*, vol. 5, no. 4, pp. 425–442, 2018.

[32] F. Renda, M. Cianchetti, M. Giorelli, A. Arienti, and C. Laschi, "A 3D steady-state model of a tendon-driven continuum soft manipulator inspired by the octopus arm," *Bioinspiration Biomimetics*, vol. 7, no. 2, 2012, Art. no. 025006.

[33] B. A. Jones, R. L. Gray, and K. Turlapati, "Three dimensional statics for continuum robotics," in *Proc. IEEE/RSJ Int. Conf. Intell. Robots Syst.*, 2009, pp. 2659–2664.

[34] K. M. de Payrebrune and O. M. O'Reilly, "On the development of rod-based models for pneumatically actuated soft robot arms: A five-parameter constitutive relation," *Int. J. Solids Struct.*, vol. 120, pp. 226–235, 2017.

[35] K. M. de Payrebrune and O. M. O'Reilly, "On constitutive relations for a rod-based model of a pneu-net bending actuator," *Extreme Mechanics Lett.*, vol. 8, pp. 38–46, 2016.

[36] K. Oliver-Butler, J. Till, and C. Rucker, "Continuum robot stiffness under external loads and prescribed tendon displacements," *IEEE Trans. Robot.*, vol. 35, no. 2, pp. 403–419, Apr. 2019.

[37] J. Fraś, J. Czarnowski, M. Maciaś, and J. Główka, "Static modeling of multisection soft continuum manipulator for stiff-flop project," in *Recent Advances in Automation, Robotics and Measuring Techniques*, R. Szewczyk, C. Zieliński, and M. Kaliczyńska, Eds., Berlin, Germany: Springer, 2014, pp. 365–375.

[38] F. Renda, F. Boyer, J. Dias, and L. Seneviratne, "Discrete Cosserat approach for multisection soft manipulator dynamics," *IEEE Trans. Robot.*, vol. 34, no. 6, pp. 1518–1533, Dec. 2018.

[39] S. M. H. Sadati, S. E. Naghibi, I. D. Walker, K. Althoefer, and T. Nanayakkara, “Control space reduction and real-time accurate modeling of continuum manipulators using Ritz and Ritz-Galerkin methods,” *IEEE Robot. Automat. Lett.*, vol. 3, no. 1, pp. 328–335, Jan. 2018.

[40] S. Grazioso, G. Di Gironimo, and B. Siciliano, “A geometrically exact model for soft continuum robots: The finite element deformation space formulation,” *Soft Robot*, vol. 6, pp. 790–811, 2018.

[41] I. S. Godage, R. Wirz, I. D. Walker, and R. J. Webster, “Accurate and efficient dynamics for variable-length continuum arms: A center of gravity approach,” *Soft Robot.*, vol. 2, no. 3, pp. 96–106, 2015.

[42] S. Sadati *et al.*, “Reduced order vs. discretized lumped system models with absolute and relative states for continuum manipulators,” in *Proc. Robot. Sci. Syst. Conf.*, 2019, Art. no. 10.

[43] J. Gerstmayr, H. Sugiyama, and A. Mikkola, “Review on the absolute nodal coordinate formulation for large deformation analysis of multibody systems,” *J. Comput. Nonlinear Dyn.*, vol. 8, no. 3, 2013, Art. no. 031016.

[44] A. A. Shabana, “An absolute nodal coordinate formulation for the large rotation and deformation analysis of flexible bodies,” Dept. Mech. Eng., Univ. Illinois, Chicago, IL, USA, Tech. Rep. MBS96-1-UIC, 1996.

[45] A. A. Shabana and R. Y. Yakoub, “Three dimensional absolute nodal coordinate formulation for beam elements: Theory,” *J. Mech. Des.*, vol. 123, no. 4, pp. 606–613, 2000.

[46] A. A. Shabana and A. E. Eldeeb, “Motion and shape control of soft robots and materials,” *Nonlinear Dyn.*, vol. 104, pp. 165–189, 2021.

[47] Q. Xu and J. Liu, “An improved dynamic model for a silicone material beam with large deformation,” *Acta Mechanica Sinica*, vol. 34, no. 4, pp. 744–753, 2018.

[48] X. Huang, J. Zou, and G. Gu, “Kinematic modeling and control of variable curvature soft continuum robots,” *IEEE/ASME Trans. Mechatronics*, vol. 26, no. 6, pp. 3175–3185, Dec. 2021.

[49] P. Polygerinos *et al.*, “Modeling of soft fiber-reinforced bending actuators,” *IEEE Trans. Robot.*, vol. 31, no. 3, pp. 778–789, Jun. 2015.

[50] J. Bishop-Moser and S. Kota, “Design and modeling of generalized fiber-reinforced pneumatic soft actuators,” *IEEE Trans. Robot.*, vol. 31, no. 3, pp. 536–545, Jun. 2015.

[51] F. Connolly, C. J. Walsh, and K. Bertoldi, “Automatic design of fiber-reinforced soft actuators for trajectory matching,” *Proc. Nat. Acad. Sci. USA*, vol. 114, no. 1, pp. 51–56, 2017.

[52] Y. C. Fung and P. Tong, *Classical and Computational Solid Mechanics*. Singapore: World Scientific, 2001.

[53] J. Bonet and R. Wood, *Nonlinear Continuum Mechanics for Finite Element Analysis*. New York, NY, USA: Cambridge Univ. Press, 2008.

[54] G. Gu, D. Wang, L. Ge, and X. Zhu, “Analytical modeling and design of generalized pneu-net soft actuators with three-dimensional deformations,” *Soft Robot.*, vol. 8, no. 4, pp. 462–477, 2021.

Xinjia Huang received the B.E. degree (with honors) in engineering mechanics from Chongqing University, Chongqing, China, in 2018. He is currently working toward the Ph.D. degree in mechanical engineering with Shanghai Jiao Tong University, Shanghai, China.

His research interests include design, modeling, and control of soft robotics.

Xiangyang Zhu (Member, IEEE) received the B.S. degree in automatic control from the Nanjing Institute of Technology, Nanjing, China, in 1985, and the M.Phil. degree in instrumentation engineering and the Ph.D. degree in control engineering, both from Southeast University, Nanjing, China, in 1989 and 1992, respectively.

From 1993 to 1994, he was a Postdoctoral Research Fellow with the Huazhong University of Science and Technology, Wuhan, China. He joined the Department of Mechanical Engineering, Southeast University, as an Associate Professor in 1995. Since June 2002, he has been with the School of Mechanical Engineering, Shanghai Jiao Tong University, Shanghai, China, where he is currently a Chair Professor and the Director with the Robotics Institute. His research interests include robotic manipulation planning, neuro-interfacing and neuro-prosthetics, and soft robotics. He has authored and co-authored more than 200 papers in international journals and conference proceedings.

Dr. Zhu was the recipient of a number of awards including the National Science Fund for Distinguished Young Scholars from NSFC in 2005, and the Cheung Kong Distinguished Professorship from the Ministry of Education in 2007. He currently serves on the editorial board of the IEEE TRANSACTIONS ON CYBERNETICS and *Bio-Design and Manufacturing*.

Guoying Gu (Senior Member, IEEE) received the B.E. degree (with honors) in electronic science and technology, and the Ph.D. degree (with honors) in mechatronic engineering from Shanghai Jiao Tong University, Shanghai, China, in 2006 and 2012, respectively.

Since October 2012, he has been working with Shanghai Jiao Tong University, where he is currently a Professor with School of Mechanical Engineering. He was a Humboldt Fellow with the University of Oldenburg, Oldenburg, Germany. He was a Visiting Scholar with the Massachusetts Institute of Technology, National University of Singapore, and Concordia University. His research interests include soft robotics, bioinspired and wearable robots, smart materials sensing, actuation, and motion control. He is the author or co-author of more than 120 publications, which have appeared in *Nature Biomedical Engineering*, *Science Robotics*, *Science Advances*, *National Science Review*, IEEE/ASME Transactions, *Advanced Materials*, *Advanced Functional Materials*, *Science Bulletin/Science China* serials, etc., as book chapters and in conference proceedings.

Dr. Gu was the recipient of the National Science Fund for Distinguished Young Scholars in 2020. He is currently an Associate Editor for IEEE TRANSACTIONS ON ROBOTICS and IEEE ROBOTICS AND AUTOMATION LETTERS. He has also served for several journals as Editorial Board Member, Topic Editor, or Guest Editor, and several international conferences/symposiums as Chair, Co-Chair, Associate Editor, or Program Committee Member.